NJC

PAPER

Heteroatom-doped core/shell carbonaceous framework materials: synthesis, characterization and electrochemical properties

Cite this: DOI: 10.1039/c8nj05193c

Yutao Zhou,[a] Qianye Huang,[b] Chee Tong John Low,[b] Richard I. Walton,[c] Tony McNally[a] and Chaoying Wan*[a]

Received 12th October 2018,
Accepted 6th March 2019

DOI: 10.1039/c8nj05193c

rsc.li/njc

Organic–inorganic hybrid core@shell nanospherical particles with a diameter of 200 nm to 600 nm were formed between cyclomatrix poly(organophosphazenes) (POP) and zeolitic imidazolate framework-8 (ZIF-8) in a methanol solution at room temperature. This facile synthesis route produced core@shell spheres with controlled structure and properties, such as mono-dispersed particles with 50 nm to 100 nm shell thickness and a surface area of 1557 $m^2\ g^{-1}$ and homogenously doped Zn and heteroatoms (N, S, P, O, Cl). The POP/ZIF-8 core@shell structures were subsequently converted into porous carbonaceous materials and investigated as anode materials in a lithium-ion coin cell battery. They showed a stable discharge capacity of 538 mA h g^{-1} over 250 cycles, high rate capability (0.1C to 1C) and excellent capacity retention, which are promising for rapid charge–discharge applications. A higher ZIF-8 loading ratio in the core@shell structure increased the capacity of the electrode materials and stabilised the lithiated active materials. The facile synthesis method and the carbonaceous framework materials are applicable for high performance energy storage materials in electrochemical power devices.

1. Introduction

Core@shell structured nanoparticles that unite different types of materials in one integrated structure at the nanoscale offer unlimited possibilities to generate synergistic and new functions. The combination of noble metal nanoparticles with inert yet porous scaffolds has the potential to extend the service life of the catalysts, reduce the product cost and improve the recyclability. Various combinations of inorganic and organic components have extended their applications in a broad range of fields, from gas storage and separation,[1] drug delivery and targeting,[2] bioimaging,[3] catalysis,[4] sensing[5] to energy materials.[6,7]

Metal organic frameworks (MOFs) offer exceptional functions for catalysis and gas separation due to their unique inorganic–organic framework structure, large surface areas (up to 3000 $m^2\ g^{-1}$) and high porosity. The formation of core–shell MOF-based structures can help overcome their susceptibility to temperature or humidity such as GO@MOF[8] (GO = graphene oxide), and also transfer the unique porosity and the catalytic properties of MOFs to other structurally stable but chemically inert materials such as SiO_2@MOF.[9] The variation in the types of materials for constructing the core or shell has made the selective functionalisation possible. Further surface treatment or morphology tuning can directly affect their properties.

The encapsulation of metallic nanoparticles within MOFs can protect the chemical reactivity of the core materials as well as inhibit the migration and aggregation of the core particles.[10,11] In addition, the MOF outlayer potentially offers high surface area, porosity, and abundant redox sites to the core/shell hybrid materials which may generate synergistic effects on catalytic, electrochemical and magnetic properties. Zeolitic imidazolate framework-8 (ZIF-8) is built from a net of tetrahedral Zn^{2+} ions connected through nitrogen in the imidazolate. It has a crystalline structure and porosity in the range of 1500–2500 $m^2\ g^{-1}$.[12] The ZIF coated SiO_2 core@shell particles with a particle size of 5 μm exhibited a surface area of 565.3 $m^2\ g^{-1}$.[9] This ZIF/SiO_2 combination utilised the column packing features of silica and the separation properties of ZIF-8, targeted to high-performance liquid chromatography for separating the endocrine-disrupting chemicals and pesticides.[9] Carbon nanotubes (CNTs) were firstly coated with a ZIF-8 layer of approximately 20 nm in thickness,[13] then transformed into CNTs@ZnO by a carbonisation treatment. The resultant

[a] International Institute for Nanocomposites Manufacturing (IINM), WMG, University of Warwick, CV4 7AL, UK. E-mail: Chaoying.wan@warwick.ac.uk; Tel: +44 (0)24 76574038
[b] Energy Innovation Centre (EIC), WMG, University of Warwick, CV4 7AL, UK
[c] Department of Chemistry, University of Warwick, CV4 7AL, UK

material showed a stable discharge capacity of 322 mA h g^{-1} at a high current density of 2000 mA g^{-1}. Metals, metal oxides and metal salts have also been integrated with MOFs to construct core/shell structures. For example, the Au@ZIF materials containing a single core or multiple cores within one ZIF shell have been reported. With Au@ZIF-8 as a photocatalyst, the oxidation conversion rate of benzyl alcohol reached 25.8% for single core materials and 51.6% for multiple core materials.[14] For energy storage applications, ZIF-8@ZIF-67 structures were transformed into carbon nanomaterials under 800 °C, where the ZIF-67 shell becomes graphitic carbon, and the ZIF-8 core becomes N-doped carbon. This approach integrates the advantages of both graphitic carbon in conductivity and heteroatoms in redox reactivity.[15] In the case of a lithium-ion battery, ZIF-8 is known to have apertures of 3.4 Å, just larger than the diameter of the Li atom (~3.0 Å) or the lithium-ion (~1.5 Å); hence structurally suitable for a diffusion process involving these species.

MOF materials have attracted increasing attention for battery and supercapacitor applications.[16–20] To date, a variety of methods have been explored to produce MOF related core@shell nanomaterials, in order to improve the structural stability, thermal stability and good electrochemical performance. Most of these methods involve complex reaction routes and multiple steps, such as plasma treatment, reflux at high temperature or hydrothermal processes,[21,22] sophisticated reaction equipment or toxic precursors. These methods generally result in 'randomly shaped building blocks'[9,15,23] with large size, instead of uniform or monodispersed structures. It is also challenging to incorporate multiple elements into one structure, thus limiting the potential for energy applications.[13] In many cases, the coating of ZIF-8 onto metal oxides or CNTs loses their crystallite nature,[13] which limits the synergistic effects.

Cyclomatrix poly(organophosphazenes) (POPs) are inorganic–organic hybrid frameworks with covalently crosslinked polymer backbones and intrinsic heteroatoms such as P, S, N and O. Nanostructured POPs can be synthesised through a rapid and facile one-pot polycondensation reaction under ambient conditions. The morphology and dimension of POPs are readily tuned from spherical, and tubular to nanosheet structures by varying their compositions and synthesis conditions. The unique covalently crosslinked structure and intrinsically doped heteroatoms (P, N, O and S) have opened great opportunities for electrochemical energy storage applications.[24] In addition, the surface of POPs with abundant functionalities such as hydroxyl, carboxyl, or amine groups,[24] offers a reactive platform for further functionalisation or structuring.[25,26] POPs have been used to form encapsulated core@shell particles for many different materials, including noble-metal particles, carbon nanotubes and graphene nanosheets,[27,28] demonstrating their synthetic versatility.

The core@shell structured ZIF particles have been reported but some unanswered problems still remain, such as wide size distribution of the resultant composites and the poor thermal stability of ZIF-8 which is sacrificed during the carbonisation process and loses the metal dopant in the composites.[29,30]

In this work, a facile synthesis route was investigated to produce POP/ZIF-8 core@shell nanospheres in a large scale at room temperature. The size of the monodispersed POP nanospheres are in the range of 200 nm, and the ZIF-8 shell is well tuned from ~20 nm to 200 nm. High surface area in excess of 1557 m^2 g^{-1} is also achieved. The POP/ZIF core@shell structure contains a transition metal and heteroatoms such as Zn, N, S and P, which are distributed homogeneously, thanks to the *in situ* synthesis process. The covalently crosslinked nanostructures offer a robust framework for the subsequent carbonisation transformation into core@shell heteroatom-doped carbonaceous structures. When applied to electrochemical power devices (*e.g.* lithium-ion batteries will be investigated in this work), these elements will help to create more reactive sites for pseudo/redox reactions[31] and increase the wettability of the electrodes, both of which can benefit the performance of the devices.

2. Experimental section

2.1 Materials

Zinc nitrate hexahydrate (98%), 2-methylimidazole (97%), sodium formate (ACS Grade), and 1-methylimidazole (99%) were purchased from VWR International Ltd (UK). Hexachlorocyclotriphosphazene (HCCP), and 4,4-sulphonyldiphenol (BPS) were purchased from Sigma-Aldrich, UK, and triethylamine (TEA) and CH_3CN were purchased from Fisher Sci, UK. All chemicals were used as received without further purification.

2.2 Synthesis of ZIF-8 particles

The synthesis of ZIF-8 crystals was based on the earlier report from Cravillon's group,[32,33] where 2-methylimidazole was excess to Zn^{2+}. Typically, 1.21 g of $Zn(NO_3)_2$ was dissolved in 40 mL MeOH, 2.03 g of 2-methylimidazole was dissolved in another 40 mL MeOH, and the two solutions were mixed together when both were fully dissolved. The mixture was then stirred for 1 h, centrifuged and washed with MeOH and then vacuum dried overnight at 60 °C.

2.3 Synthesis of POP nanospheres

121.8 mg HCCP and 277.8 mg BPS were added to 200 mL acetonitrile while sonicating, and 3 mL TEA was added to the mixed solution after 5 minutes, and sonication was maintained for 1 h. The mixture was then centrifuged and washed with acetone before being vacuum-dried overnight at 60 °C.

2.4 Synthesis of POP/ZIF core@shell structure

A typical synthesis process is described briefly here, consider the sample A given in Table 1 as an example. 50 mg POP was dispersed in 55 mL of MeOH under sonication for 2 h, then 0.90 g $Zn(NO_3)_2{\cdot}6H_2O$ was added. Then 1.51 g of 2-methylimidazole was added to the POP solution and stirred for 5 min. The solution was allowed to stand for 24 h, then centrifuged and washed with MeOH before being vacuum-dried

Table 1 Reaction conditions for synthesis of POP/ZIF core/shell particles (samples A–F)

Sample	POP (g)	Zn^{2+} (g)	2-MI (g)	MeOH (mL)	Reaction time (h)	POP/ZIF-8 weight ratio
A	0.05	0.60	1.01	32 × 2	24	1 : 2.5
B	0.05	0.60	1.01	32 × 2	48	1 : 2.5
C	0.05	0.60	1.01	20 × 2	24	1 : 2.5
D	0.05	0.97	1.62	32 × 2	24	1 : 4
E	0.05	1.44	2.40	48 × 2	24	1 : 6
F	0.05	1.92	3.20	64 × 2	24	1 : 8

overnight at 60 °C. The variation of the synthesis conditions are listed in Table 1.

2.5 Structural characterisation

Field emission gun-scanning electron microscopy (FEG-SEM) and X-ray electron dispersive spectroscopy (EDS) analyses were accomplished using a Zeiss SIGMA SEM. The gold–palladium sputtering was applied to the uncarbonised samples before analysis. The carbonised samples needed no coating due to their high electrical conductivity. Raman spectra were obtained using a Renishaw inVia spectrometer equipped with a 532 nm laser. Thermogravimetric analyses were recorded using a Mettler Toledo instrument in the temperature range of 25–850 °C at a heating rate of 10 °C min^{-1} under N_2 gas flow (30 mL min^{-1}). Specific surface areas were calculated from the nitrogen adsorption–desorption isotherm curves recorded using a Micromeritics ASAP 2020 Physisorption Analyzer (0.0–1.0P/P_0). The samples were degassed at 120 °C for 3 hour under high vacuum before measurements. The powder X-ray diffraction (XRD) patterns were obtained using a Panalytical Empyrean diffractometer with a CoKα radiation source (1.7929 Å) operated at 40 kV and 40 mA. The scanning step was 0.013° 2θ.

2.6 Electrochemical characterisation

For electrochemistry analysis, a slurry paste containing the carbonised POP/ZIF-8 (850 °C, 73 wt%, sample A or F), carbon black (18 wt%) and a PVDF binder (9 wt%) was prepared in a *N*-methyl-2-pyrrolidone (NMP) solvent. The slurry was casted on copper foil (as energy storage electrode) with a blade gap of 80 μm, which was then dried overnight in a vacuum oven before assembling into a coin cell (type 2032 format). Half-cells were constructed using lithium foil as the reference and counter electrodes. Celgard 2325 microporous membrane was used as the separator material. 1 M $LiPF_6$ in ethylene carbonate : ethylmethyl carbonate (3 : 7 volume ratio) and 1 wt% vinylene carbonate was used as the electrolyte.

Electrochemical impedance spectroscopy (EIS) was used to measure the impedance change along with cycle numbers. The test was conducted with a voltage amplitude of 10 mV, measured between frequencies of 400 kHz and 100 MHz at a fully lithiated state of each cell. The first measurement was taken after the formation cycle with an additional relaxation time of 10 min, and then repeated every 20 cycles.

3. Results and discussion

ZIF-8 coated POP nanospheres are synthesised by following the formulation shown in Table 1. $Zn(NO_3)_2{\cdot}6H_2O$ was firstly mixed with POP in MeOH. This is to allow the $Zn(NO_3)_2{\cdot}6H_2O$ to fully adsorb onto the POP surfaces through hydrogen bonding with the abundant hydroxyl groups of POPs.[34,35] A layer of ZIF-8 crystals was formed on the POP surface after the subsequent addition of 2-methylimidazole (Hmim) to the dispersion.

The morphologies of POPs, ZIF-8 and POP/ZIF nanostructures are shown in Fig. 1. The POPs are in the form of spheres with a diameter of approximately 200 nm (Fig. 1A). The ZIF-8 crystals synthesised under the same conditions as sample A (Table 1) appear as cubes of approximately 40–50 nm as shown in Fig. 1B. The core/shell POP/ZIF particles are shown in Fig. 1C, a layer of ZIF-8 crystals of 40–50 nm was observed on the POP surface from the inset image, and a gap was observed between the POP core and the ZIF-8 shell suggesting that the presence of POP spheres does not affect the formation of ZIF-8 crystals, and each material maintains its structural independence.

The structure of sample A was investigated by powder XRD and FT-IR spectroscopy. As shown in Fig. 3a, the ZIF-8 shell of the POP/ZIF particles exhibits the same characteristic diffraction patterns as the original ZIF-8 crystal,[36] which confirm the integrity of ZIF-8 in the POP/ZIF structure. According to the FT-IR results shown in Fig. 3b, the absorbances at 1585 cm^{-1} and 1487 cm^{-1} arise from the C=C stretching vibration of the POPs, the band at 1292 cm^{-1} is the S=O=S stretch from the BPS, the band at 1180 cm^{-1} is the P=N stretch from the HCCP,

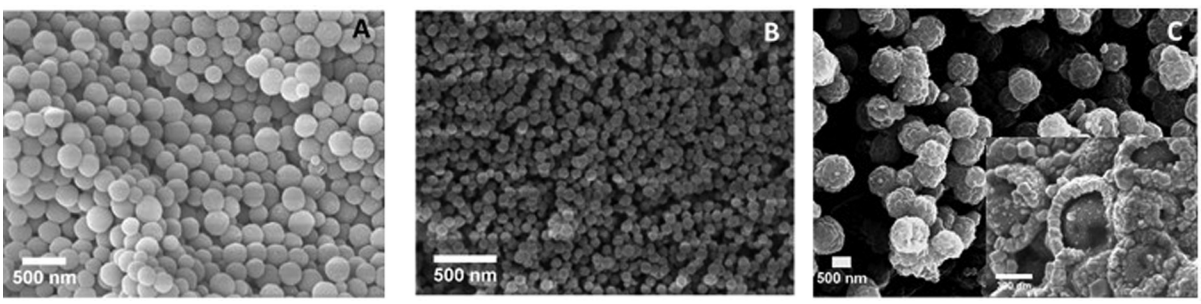

Fig. 1 SEM images of (A) POPs nanospheres, (B) ZIF-8 particles and (C) POP/ZIF core@shell structure (sample A) with an inset image showing the shell thickness.

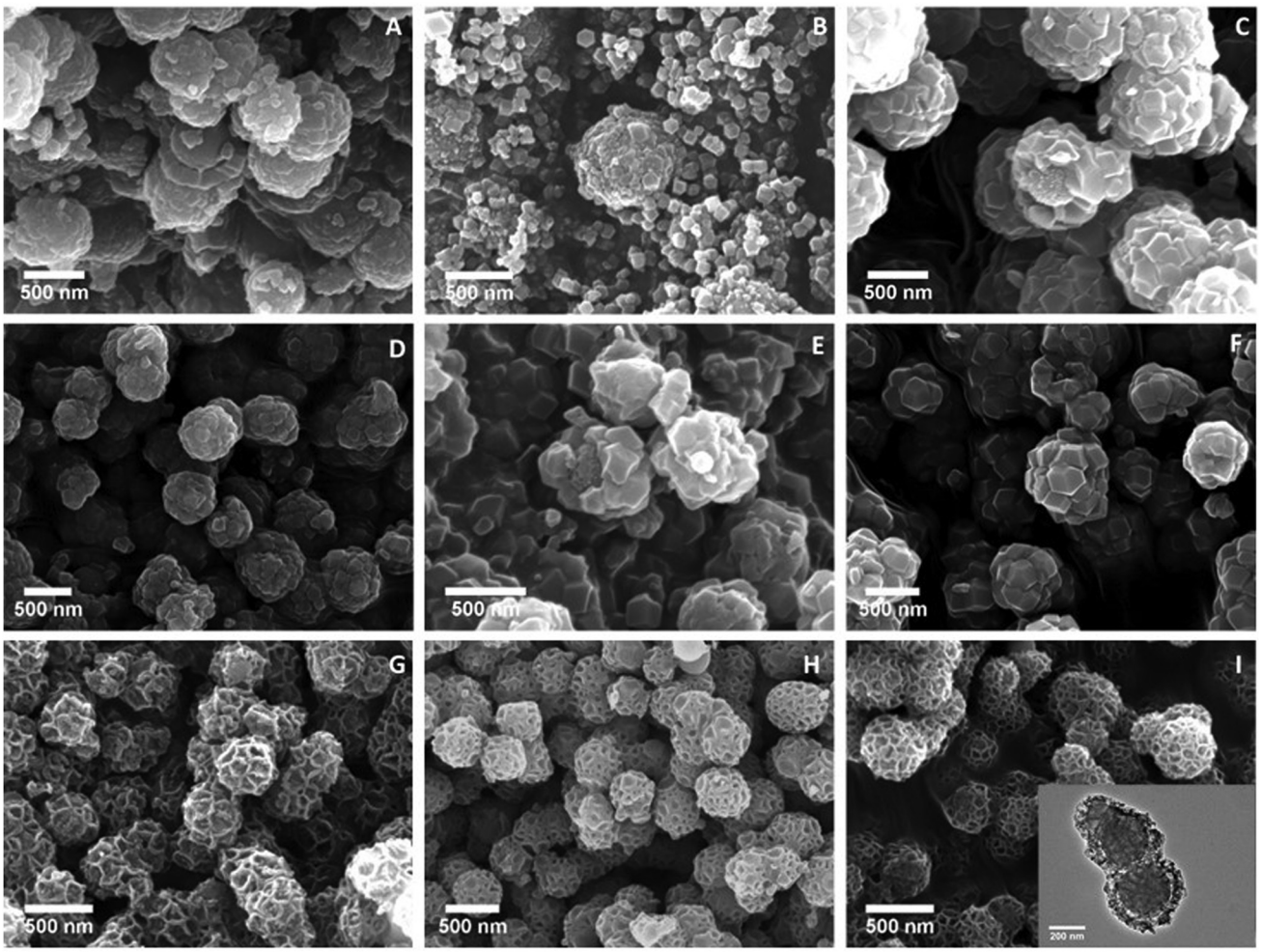

Fig. 2 Morphology of POP/ZIF-8 core/shell nanospheres of sample (A to F) and carbonized (G) sample (D and H) sample (E and I) sample (F).

and the band at 933 cm^{-1} is the P–O–C stretch. For ZIF-8, the band at 1579 cm^{-1} can be assigned to the C═N stretching mode, and the band at 1624 cm^{-1} is attributed to the C═C vibration absorption of the ZIF-8.[37] The absorption bands in the 1100–1400 cm^{-1} region are associated with the C–N stretch.[38] Both powder XRD and FTIR results indicate that the characteristic features of the original ZIF-8 and POPs were maintained in the POP/ZIF-8 structure, which confirms the structural independence and stability of both the POP and ZIF-8 particles in the core@shell structure.

The porosimetry results in Fig. 3c show a typical microporous structure for both ZIF-8 and POP/ZIF-8. The ZIF-8 shows a BET surface area of 251 $m^2 g^{-1}$, and a Langmuir surface area of 1930 $m^2 g^{-1}$. The POP/ZIF core@shell particles reach a single point surface area of 1070 $m^2 g^{-1}$ with the Langmuir surface area of 1557 $m^2 g^{-1}$. The POP has a BET surface area of 19 $m^2 g^{-1}$ measured in our previous work,[39] therefore the coating of a layer of ZIF-8 crystals significantly increased the specific surface area of the POP spheres, and extended its potential for electrochemical applications.

The morphology and dimension of POP/ZIF-8 core/shell particles can be tuned by varying the composition ratios and reaction conditions. The different conditions for samples A–F are shown in Table 1.

3.1 Reaction time

The synthesis conditions for sample A (Fig. 1C) are used as a control. As shown in Table 1, sample B has the same composition ratio as sample A but with an extended reaction time of 48 h. As characterised by SEM (Fig. 2B), sample B has bigger ZIF-8 particles formed on the surface, with a size of ~100 nm and a wider particle size distribution and some free ZIF-8 particles are also observed. This indicates that the particle size and distribution of ZIF-8 are increased with reaction time.

It was reported that the nucleation and individual crystal growth of ZIF-8 occur simultaneously.[32] At the early stage of the reaction, the nucleation dominates and generates a large number of small crystals. When the Hmim concentration is excess to the Zn^+ concentration, the neutral Hmim can create positive surface charges, and terminate the formation of the ZIF-8. After the nucleation and growth reaction are terminated, the small particles tend to aggregate into larger ones with extended reaction time.[32,40,41] This may explain the larger particle size and distribution of sample B than sample A.

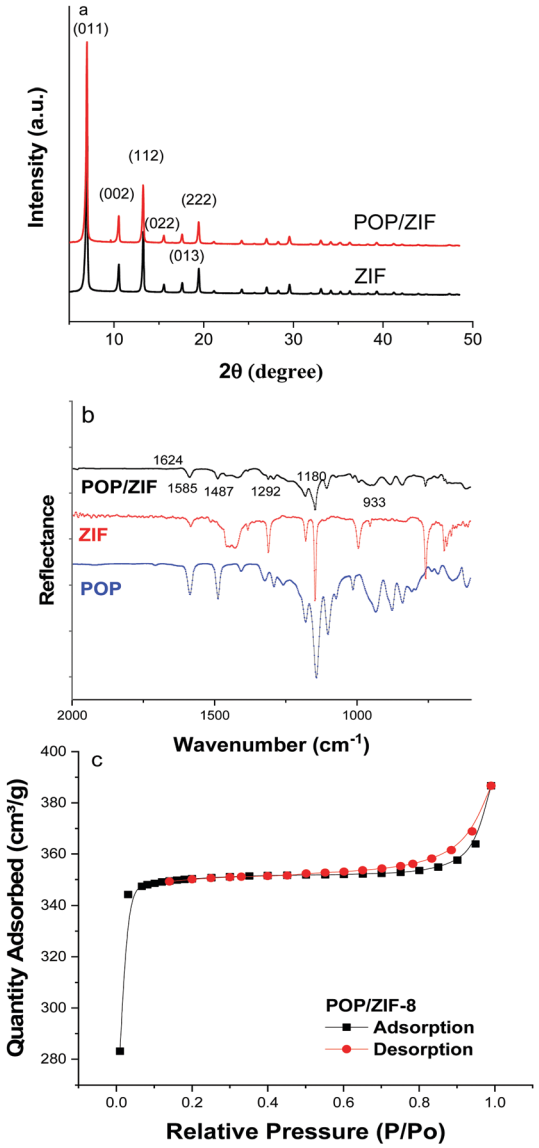

Fig. 3 (a) Powder XRD patterns of ZIF-8 and sample A; (b) FT-IR results of POP, ZIF-8 and sample A; and (c) porosimetry results of sample A.

3.2 Reactant concentration

Sample C was synthesised using the same composition as sample A, but with less methanol solvent (40 mL). The higher reactant concentration resulted in a lower yield and larger size of the ZIF-8 particles, as shown in Fig. 2C. To compare the effect of the POP/ZIF-8 ratio, the amount of POPs was fixed as 50 mg and the reaction time was fixed as 24 h. The ZIF-8 loading ratios of POPs : ZIF-8 were varied from 1 : 4 (sample D), 1 : 6 (sample E) to 1 : 8 (sample F). As shown in Fig. 2D–F, more $Zn(NO_3)_2{\cdot}6H_2O$ and 2-methylimidazole resulted in larger ZIF-8 crystals on the POP surface. As the shell is formed by one single layer of ZIF-8 particles, the shell thickness of samples D, E and F is increased to ~50 nm, ~100 nm and ~200 nm, respectively. Meanwhile, the shape of the ZIF-8 crystals changes from small cubes to rhombic dodecahedra with a wider size distribution.

These observations can be explained by the following reaction mechanism. The Hmim acts as both the bridging unit and structure stabilizer of ZIF-8 when it is neutral.[33] The Hmim addition is excess to that of the Zn^{2+}, and therefore results in a high nucleation rate at the beginning of the reaction. At the later stage, the formation of ZIF-8 can be stopped as enough neutral Hmim stabilizes the nanocrystals with the accumulated positive surface charges[33] against the deprotonated Hmim. In the presence of POPs, the reaction preferably takes place on the surface of the POPs instead of in the solution, due to the hydrogen bonding interactions between $Zn(NO_3)_2{\cdot}6H_2O$ and the abundant hydroxyl groups of POPs. With the increase of $Zn(NO_3)_2{\cdot}6H_2O$ and 2-methylimidazole amounts, more Zn^{+} is absorbed on the POP surface than in the solution. The relatively excess Hmim can still accelerate the nucleation rate of ZIF-8 on the POP surface, and the Hmim around Zn^{2+} can be lower than that in the reaction solution without POP. The relatively lower concentration of Hmim near the surface of POPs, along with the fast formation reaction on the POP surfaces which introduces more side products can determine the final ZIF-8 particle sizes. These side products can slow down the deprotonation of Hmim or the formation of ZIF-8 by competing with Hmim. These factors have resulted in a lower nucleation rate and a larger crystal size.

3.3 Carbonisation

The POP/ZIF-8 core/shell nanostructures of samples D, E and F were carbonised at 850 °C for 1 h and the morphologies were characterised by SEM as shown in Fig. 2G–I. The POP/ZIF organic–inorganic core/shell nanospheres were transformed into carbon materials with a well-preserved spherical morphology. At different POP : ZIF ratios, the samples D, E and F are all uniformly covered with raspberry shape surface layers, some small cubic-shaped particles are still visible in the shell structures. This shows clearly that the core@shell structure is well maintained and the POP core can be observed under the carbonised ZIF-8 streak shell. With more ZIF-8 addition (POP/ZIF-8, 1 : 8 wt%, sample F), the carbonised shells are more compact, and more streaks are formed on the surface. This indicates that the POP core and ZIF-8 shell are carbonised at the same time without interfering each other, and maintained the core@shell structures at 850 °C. This also reflects the high thermal stability of the core@shell structure during the carbonisation process, and there is a perfect balance between the independence and the combination of the core and shell materials.

As examined by EDS, sample F originally has atoms of C (50.9%), N (26.1%), and Zn (13.6%), and other heteroatoms P and S of 0.2% (details showed in Table 2). After carbonisation, Zn becomes the main element of 35.5%, the carbon skeleton reduces to 21.0%, both N and P remain at 13.5% and 3.5%, and S and Cl remain at 0.5% and 0.7%, respectively. The weight ratios of the metal and heteroatoms are increased as a result of the loss of carbon. The obtained carbonaceous samples were rich in Zn and the heteroatoms N, P and S. When comparing POP/ZIF-8 = 1 : 2.5 (sample A) with 1 : 8 (sample F), the

Table 2 EDS results of samples A and D

	Sample A		Sample F	
	wt%			
Element	Original	850 °C	Original	@850 °C
C	69.4	57.4	50.9	21.0
N	13.0	0.0	26.1	13.5
Zn	3.9	10.7	13.6	35.5
O	13.4	21.2	9.1	25.4
P	0.0	4.8	0.2	3.5
S	0.0	0.7	0.2	0.5
Cl	0.3	0.0	0.0	0.7

dominant elements in ZIF-8 are Zn and N, and the weight ratio of Zn/N in sample F is significantly higher than that in sample A, even after carbonisation. These results showed that the POP nanospheres are stable carriers for ZIF-8, and the hydrogen bonding interactions between $Zn(NO_3)_2{\cdot}6H_2O$ and the abundant hydroxyl groups of POPs are strong enough to carry a high amount of ZIF-8.

Porosimetry results changed significantly before and after carbonisation for both the core@shell structure and their components, the original POP spheres showed a low surface area of 19 $m^2\ g^{-1}$, and transformed into porous carbon spheres with a higher surface area up to 937 $m^2\ g^{-1}$ after carbonisation at 850 °C. The carbonisation process triggered the formation of micropores in POP.

After carbonisation, the surface area of POP/ZIF-8 (sample A) decreased from 1557 $m^2\ g^{-1}$ to 16 $m^2\ g^{-1}$. Similar results were obtained in CNTs/ZIF core@shell structures, where the surface area of the CNTs/ZIF dropped to below 80 $m^2\ g^{-1}$ after carbonisation.[13] The ZIF-8 starts to collapse from 500 °C (shown in Fig. 5a by the onset of mass loss in the TGA), so the degradation of ZIF-8 accounts for the reduced surface area of the carbonised core/shell structures. As shown in Fig. 2, after carbonisation, the ZIF-8 shells shrank and wrapped tightly onto the spherical cores. The POP/ZIF-8 with different shell thicknesses showed different morphologies after carbonisation. The decomposed ZIF-8 particles might block the micro pores of the carbonised POP cores, therefore resulted in a lower surface area for the carbonised core/shell particles. The powder XRD shown in Fig. 5b also shows that the ZIF-8 shell in the core@shell structure loses its crystalline structure after carbonisation at 850 °C. As characterised by Raman spectroscopy, shown in Fig. 5c, the G and D bands are observed at 1350 cm^{-1} and 1590 cm^{-1}. The D band shows the in-plane defects or heteroatoms/metal doping that results from sp^2-hybridised carbon disorder, while the G band shows the existence of crystalline graphitic carbon.[42] Further analysis, by peak area determination, shows that the sample is made up of 71% of amorphous carbon and 29% of graphitic carbon. The graphitic carbon could originate from the Hmim ligands in the ZIF-8. By decomposing the C–N bonds, the Hmim were transformed to graphitic carbon from amorphous carbon.[43]

3.4 Electrochemical analysis

The carbonised POP/ZIF-8 core/shell structures containing high Zn and heteroatom (S, P, N) contents are promising for

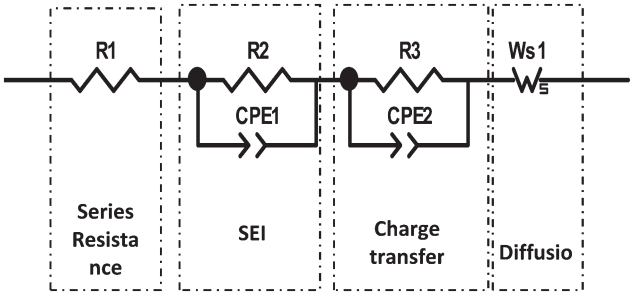

Fig. 4 The equivalent circuit for fitting the impedance spectra.

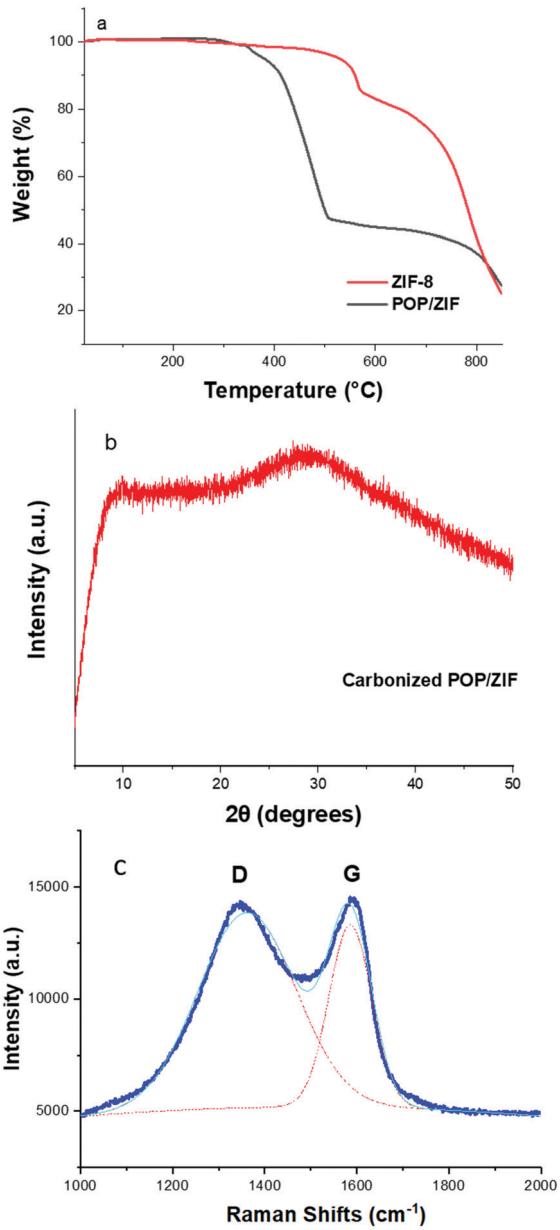

Fig. 5 (a) TGA results of POP/ZIF (sample A) and ZIF-8; (b) powder XRD pattern of carbonized sample A and (c) Raman result of carbonized sample A.

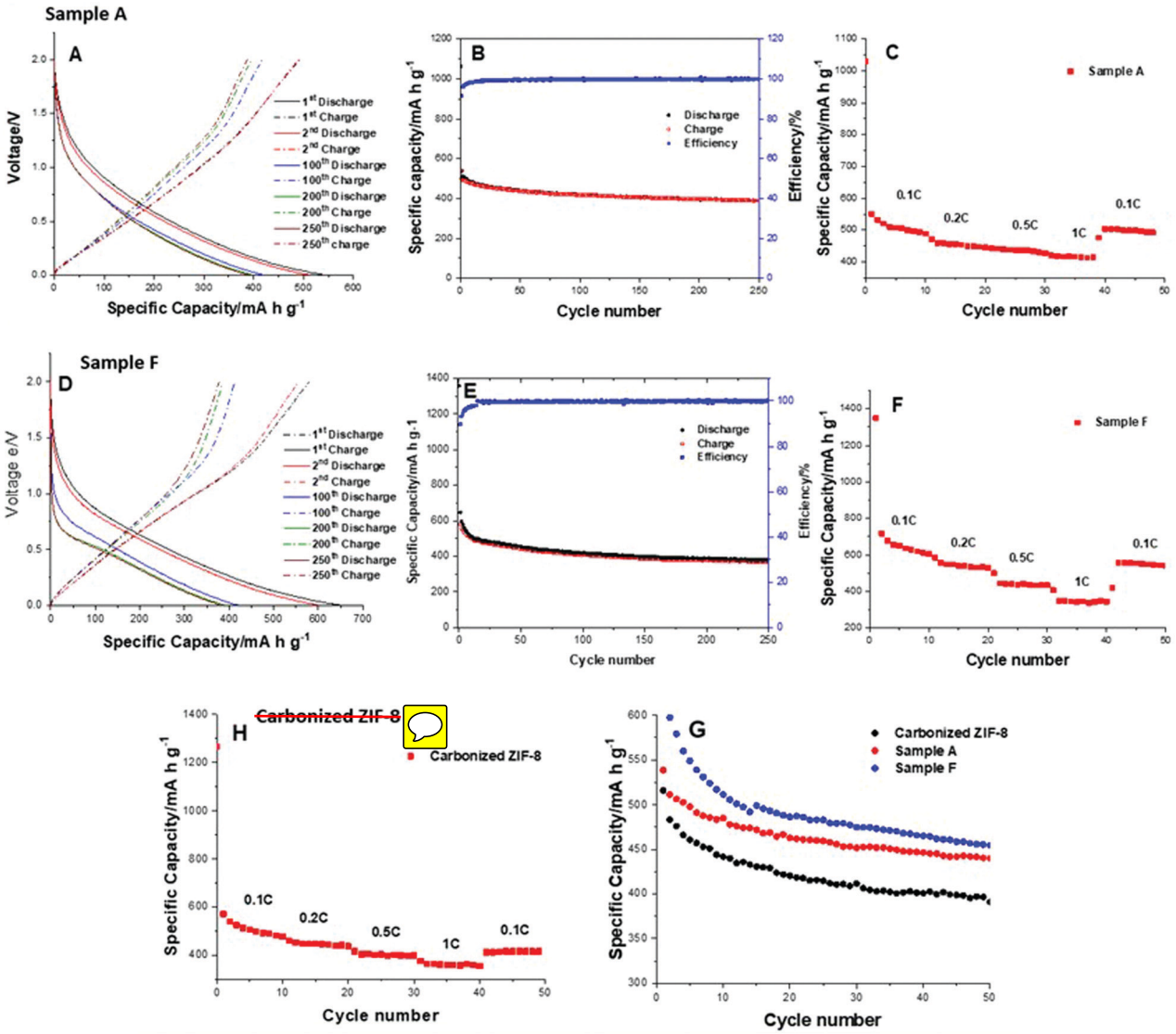

Fig. 6 (A) Successive charge and discharge cycles; (B) long-term cyclability; and (C) rate capability performance of carbonised sample A; and (D) successive charge and discharge cycles; (E) long-term cyclability; and (F) rate capability performance of carbonised sample F; (G) capacity performance comparison between sample A, F and pure ZIF-8; (H) rate capability performance of pure carbonized ZIF-8.

electrochemical energy storage applications. To further investigate the synergistic effect of the core@shell structure and the heteroatom contents on the electrochemical properties of the materials, comparison studies were carried out between sample A and sample F.

Based on the EIS spectra of the electrodes, the fitting equivalent circuit is shown in Fig. 4. It consists of a resistor representing series resistance and is followed by a series of three resistors in parallel with constant phase elements and a Warburg diffusion element at the end. They respectively account for the SEI resistance, charge transfer resistance and diffusion impedance.

The coin cell was firstly subjected to a series of charge and discharge cycles. A total of 250 cycles were performed (see Fig. 6). The operating window of cell voltage was set between 0.01 and 2.0 V *vs.* Li/Li^+, and a current density at 74 mA g^{-1} (based on the mass of active materials) was used. For sample A, the 1st cycle recorded 493 mA h g^{-1} charge capacity and 538 mA h g^{-1} discharge capacity, which were consistent with the typical findings[44] for Li-ion insertion and solid electrolyte interface formation on the anode material of a Li-ion battery. For sample F, the 1st cycle recorded 580 mA h g^{-1} charge capacity and 647 mA h g^{-1} discharge capacity. The recorded specific capacity (both charge and discharge) of a carbonaceous framework materials was higher than the theoretical capacity of the graphite anode (372 mA h g^{-1})[45] in a Li-ion battery, and the cycling curves stabilised towards the later part of 250 cycles. The increased capacity could benefit from the rich heteroatom content and transit metal content that help to create more reactive sites for the pseudo/redox reaction that could all contribute to the capacity. Sample F has a higher ZIF weight ratio than sample A, the increased capacity proved the synergistic effect, and the

greater structural stability and capability of carrying higher ZIF particles in the structure even after the carbonization of sample F. The above results prove that the presence of heteroatoms and transition metal elements benefits the electrochemical performance of the core@shell nanoparticles based electrodes.

Fig. 6B and E show the discharge capacity (mA h g^{-1}) and coulombic efficiency (%) of the constant current cycling profile of both sample A and F. The recorded capacities steadily dropped to a lower value during the earlier part of cycling, which was a typical observation due to solid electrolyte interphase (SEI) formation on the anode material of Li-ion battery. Towards the latter part of 250 cycles, cycling data recorded a reversible 388/400 mA h g^{-1} charge and discharge capacities (*i.e.* 100% coulombic efficiency). The higher ZIF-8 loading ratio to the core@shell structure can increase the anode capacity and cycling stability over time;[46] hence offering materials with enhanced anode performance for lithiation and de-lithiation processes in Li-ion batteries. Fig. 6C shows power extraction capability of the carbonized sample A. The recorded discharge capacities were: 500 mA h g^{-1} (0.1C start first), 460 mA h g^{-1} (0.2C), 440 mA h g^{-1} (0.5C), 420 mA h g^{-1} (1C) and 490 mA h g^{-1} (finish back to 0.1C). The coin cell (at high 1C-rate) still remains at 84% of its initial capacity. This suggests that the carbonisation treatment and ZIF-8 derived porous carbon structure might enhance the Li-ion diffusion, resulting in a robust electrochemical activity upon high power extraction. When the coin cell was cycled back using 0.1C, the recorded capacity showed 490 mA h g^{-1} with a capacity retention of 98%; this suggests the excellent cycling stability across a range of power extraction values.

Fig. 6F shows the power extraction capability of carbonized sample F: 620 mA h g^{-1} (0.1C start first), 540 mA h g^{-1} (0.2C), 440 mA h g^{-1} (0.5C), 344 mA h g^{-1} (1C) and 550 mA h g^{-1} (finish back to 0.1C). Sample F showed a better capacity compared to sample A which again proves the synergistic effect and the contribution to the electrochemical performance of carbonized ZIF-8 in the structure. Sample F also showed good rate stability with a capacity retention of 89% of its initial capacity.

Carbonized ZIF-8 sample was analyzed under the same condition for comparison. It was reported that carbonized ZIF-8 as the electrode in the Li-ion battery suffered fast capacity fade within the first 10 cycles.[47] In Fig. 6G, the capacity of pure carbonized ZIF-8, sample A (2.5 : 1) and sample F (8 : 1) in the first 50 cycles are compared. It is clear that sample F containing the highest ZIF-8 loading ratio showed the highest capacity throughout the test. The carbonized ZIF-8 showed the lowest capacity and a rapid fading rate. At cycle 50, the capacity of sample F was 454 mA h g^{-1}, while 439 mA h g^{-1} for sample A and 391 mA h g^{-1} were observed for carbonized ZIF-8.

The core@shell structure exhibited better performance than carbonized ZIF-8 or carbonized POP alone. The capacity of carbonized POP-based electrodes in Li-ion batteries was measured to be 300 mA h g^{-1} at the early cycles and 130 mA h g^{-1} after 1000 cycles.[39] The results showed that the ZIF/POP core@shell structure not only avoided the rapid capacity fading but also improved the performance of POP. The POP spheres supported the growth of ZIF-8 and helped to stabilize the carbonised ZIF-8 structure. The remaining heteroatoms and Zn in the ZIF-8 also benefit the capacity improvement.

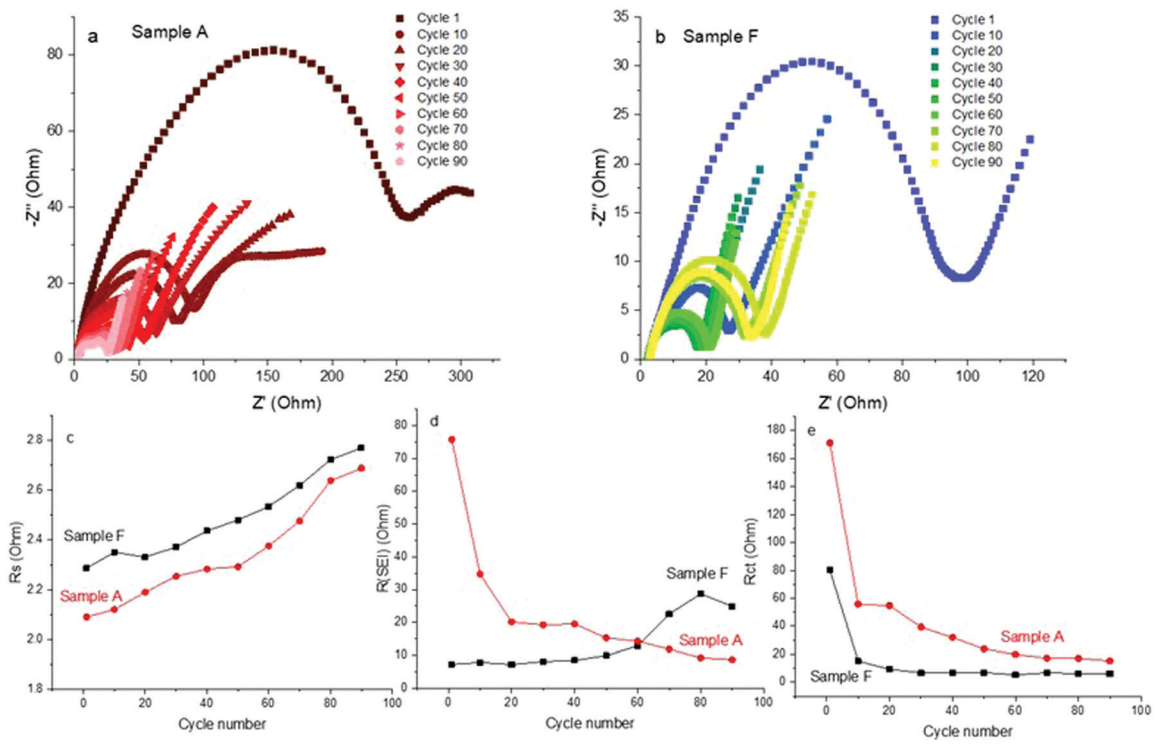

Fig. 7 Nyquist impedance spectra of (a) sample A and (b) sample F over cycling; the impedance fitting result of (c) series resistance, (d) SEI resistance and (e) charge transfer resistance.

Carbonized ZIF-8 materials could barely retain the capacity of 300 mA h g^{-1} just after the first 50 cycles as previously reported.[47] The ZIF-8 derived CNTs@$ZnCoO_2$ materials with excess Co showed an initial charge capacity of 435.6 mA h g^{-1},[13] which was lower than that of the carbonized POP/ZIF materials of 538 mA h g^{-1} with stability over 250 cycles. The better cyclability and higher capacity of the carbonised POP/ZIF core@shell structures can be ascribed to the well-maintained framework structures after thermal treatment compared to previous reported materials; the *in situ* doped heteroatoms and transition metal Zn created more redox-active sites and improved the wettability of the anode material.[48] In the rate performance test, the capacity of the half-cell can reach back to 460 mA h g^{-1} after 0.5C, exhibiting good stability after higher current cycling, and great potential for fast charge–discharge devices. Fig. 7a and b show the Nyquist curves over cycling for sample A and sample F, indicating the variation trend of impedance. The fitting results are summarized in Fig. 7c–e, which are in correspondence to the Nyquist data. It can be observed from Fig. 7c that the sample A-based electrode shows a relatively low series resistance, indicating a slightly better ionic conductivity in general compared to sample F. This agrees with the rate capacity results. Fig. 7d shows that there is massive SEI resistance ($\sim$75 Ohm) for sample A initially due to a larger surface area, then the SEI resistance dramatically reduces to 20 Ohm after 20 cycles and gradually decreases over cycling. It suggests that the SEI for sample A is slowly stabilised over cycling, however, this slow process may cause more irreversible capacity loss. In contrast, for electrodes with sample F, the SEI resistance is much lower and more stable for first 60 cycles. It starts to grow afterwards possibly due to the electrolyte aging effect. For both materials, the charge transfer will be largely reduced after 10 cycles (Fig. 7e), by which point, most active particles have been fully lithiated and it becomes easier for the particle surface to transfer Li ions. Similarly to the SEI resistance, it has been observed that for sample A, the charge transfer resistance is slowly reduced until it stablises from cycle 10 to cycle 90, which indicates that it takes much longer for sample A to reach a stable lithiated phase.

4. Conclusions

A facile and rapid synthesis method to produce POP/ZIF core@shell nanospheres at room temperature is investigated. This core@shell structure provides a high surface area, rich heteroatom and metal content. The core/shell particle dimensions are facilely tuned by varying the reaction conditions such as reaction time and reactant ratios. The ZIF-8 crystals are increased from 40 nm to 200 nm and form a thicker shell on POP spheres when the reaction time is increased from 24 h to 48 h; and by increasing the ZIF-8 loadings to the POP spheres from 2.5 : 1 to 8 : 1, the particle size of ZIF-8 can be enlarged from 50 nm to 300 nm; in both ways they showed the flexibility of the structure and content, which exhibited the potential for different applications. The core@shell structures are well maintained after carbonisation at 850 °C demonstrating a high thermal stability of the framework structures. The core@shell carbon structure reaches a capacity of 538 mA h g^{-1}, with retention of 79% after 250 cycles. A high capacity retention of 98% in rate capability performance also showed excellent cycling stability across a range of power extraction values. With a higher ZIF-8 loading ratio in the core@shell structure, the electrochemical performance was much improved. In comparison with a pure ZIF-8 or pure POP material, the core@shell structure showed significantly better electrochemical performance. The electrochemical impedance spectroscopy proves that the higher ratio of ZIF-8 could assist the active particle to be lithiated to a stable phase and maintain the internal resistance at a stable level. The characterisation and electrochemical tests indicate the excellent synergistic effects between ZIF-8 and POP that promote the performance of the electrodes. The present work explores a facile method to design and produce structurally stable and electrochemically active electrode materials for energy storage applications.

Conflicts of interest

There are no conflicts to declare.

References

1 Q. Yue, Y. Zhang, Y. Jiang, J. Li, H. Zhang, C. Yu, A. A. Elzatahry, A. Alghamdi, Y. Deng and D. Zhao, *J. Am. Chem. Soc.*, 2017, **139**, 4954–4961.
2 C. Song, M. Yang, D. Wang and Z. Hu, *Mater. Res. Bull.*, 2010, **45**, 1021–1025.
3 W. Tan, K. Wang, X. He, X. J. Zhao, T. Drake, L. Wang and R. P. Bagwe, *Med. Res. Rev.*, 2004, **24**, 621–638.
4 L. Feng, G. Gao, P. Huang, K. Wang, X. Wang, T. Luo and C. Zhang, *Nano Biomed. Eng.*, 2010, **2**, 258–267.
5 L. Stanciu, Y.-H. Won, M. Ganesana and S. Andreescu, *Sensors*, 2009, **9**, 2976–2999.
6 K. M. Choi, H. M. Jeong, J. H. Park, Y.-B. Zhang, J. K. Kang and O. M. Yaghi, *ACS Nano*, 2014, **8**, 7451–7457.
7 A. Pajor-Świerzy, Y. Farraj, A. Kamyshny and S. Magdassi, *Colloids Surf., A*, 2017, **522**, 320–327.
8 J. Wang, Y. Wang, Y. Zhang, A. Uliana, J. Zhu, J. Liu and B. Van der Bruggen, *ACS Appl. Mater. Interfaces*, 2016, **8**, 25508–25519.
9 Y.-Y. Fu, C.-X. Yang and X.-P. Yan, *Chem. – Eur. J.*, 2013, **19**, 13484–13491.
10 H.-L. Jiang and Q. Xu, *Chem. Commun.*, 2011, **47**, 3351–3370.
11 H.-L. Jiang, B. Liu, T. Akita, M. Haruta, H. Sakurai and Q. Xu, *J. Am. Chem. Soc.*, 2009, **131**, 11302–11303.
12 H.-L. Jiang and Q. Xu, *Chem. Commun.*, 2011, **47**, 3351–3370.
13 G. Huang, D. Yin and L. Wang, *J. Mater. Chem. A*, 2016, **4**, 15106–15116.
14 L. Chen, Y. Peng, H. Wang, Z. Gu and C. Duan, *Chem. Commun.*, 2014, **50**, 8651–8654.

15 J. Tang, R. R. Salunkhe, J. Liu, N. L. Torad, M. Imura, S. Furukawa and Y. Yamauchi, *J. Am. Chem. Soc.*, 2015, **137**, 1572–1580.

16 Y. Zhao, Z. Song, X. Li, Q. Sun, N. Cheng, S. Lawes and X. Sun, *Energy Storage Mater.*, 2016, **2**, 35–62.

17 F.-S. Ke, Y.-S. Wu and H. Deng, *J. Solid State Chem.*, 2015, **223**, 109–121.

18 W. Liu and X.-B. Yin, *TrAC, Trends Anal. Chem.*, 2016, **75**, 86–96.

19 L. Wang, Y. Han, X. Feng, J. Zhou, P. Qi and B. Wang, *Coord. Chem. Rev.*, 2016, **307**, 361–381.

20 G. Xu, P. Nie, H. Dou, B. Ding, L. Li and X. Zhang, *Mater. Today*, 2017, **20**, 191–209.

21 N. Zhang, B. Zhu, F. Peng, X. Yu, Y. Jia, J. Wang, L. Kong, Z. Jin, T. Luo and J. Liu, *Chem. Commun.*, 2014, **50**, 7686–7689.

22 P. Xu, H. Wang, R. Lv, Q. Du, W. Zhong and Y. Yang, *J. Polym. Sci., Part A: Polym. Chem.*, 2006, **44**, 3911–3920.

23 H. Tian, J. Liu, K. O'Donnell, T. Liu, X. Liu, Z. Yan, S. Liu and M. Jaroniec, *J. Colloid Interface Sci.*, 2016, **476**, 55–61.

24 C. Wan and X. Huang, *Mater. Today Commun.*, 2017, **11**, 38–60.

25 H. Ozay and O. Ozay, *Colloids Surf., A*, 2014, **450**, 99–105.

26 Z. Huang, S. Chen, X. Lu and Q. Lu, *Chem. Commun.*, 2015, **51**, 8373–8376.

27 J. Fu, X. Huang, Y. Huang, Y. Pan, Y. Zhu and X. Tang, *J. Phys. Chem. C*, 2008, **112**, 16840–16844.

28 J. Fu, X. Huang, Y. Huang, J. Zhang and X. Tang, *Chem. Commun.*, 2009, 1049–1051.

29 W. Ma, N. Wang, T. Tong, L. Zhang, K.-Y. A. Lin, X. Han and Y. Du, *Carbon*, 2018, **137**, 291–303.

30 S. Yang, L. Peng, P. Huang, X. Wang, Y. Sun, C. Cao and W. Song, *Angew. Chem.*, 2016, **128**, 4084–4088.

31 K. N. Wood, R. O'Hayre and S. Pylypenko, *Energy Environ. Sci.*, 2014, **7**, 1212–1249.

32 J. Cravillon, R. Nayuk, S. Springer, A. Feldhoff, K. Huber and M. Wiebcke, *Chem. Mater.*, 2011, **23**, 2130–2141.

33 J. Cravillon, S. Münzer, S.-J. Lohmeier, A. Feldhoff, K. Huber and M. Wiebcke, *Chem. Mater.*, 2009, **21**, 1410–1412.

34 Y. Han, H. Huang, H. Zhang, Y. Liu, X. Han, R. Liu, H. Li and Z. Kang, *ACS Catal.*, 2014, **4**, 781–787.

35 F. Niu, L. Zhang, S.-Z. Luo and W.-G. Song, *Chem. Commun.*, 2010, **46**, 1109–1111.

36 N. Nordin, A. Ismail, A. Mustafa, P. Goh, D. Rana and T. Matsuura, *RSC Adv.*, 2014, **4**, 33292–33300.

37 ~~X. Gao, X. Hai, H. Baigude, W. Guan and Z. Liu, *Fabrication of functional hollow microspheres constructed from MOF shells: Promising drug delivery systems with high loading capacity and targeted transport*, 2016.~~

38 J. B. James and Y. S. Lin, *J. Membr. Sci.*, 2017, **532**, 9–19.

39 G. Pappas, S. Ferrari, X. Huang, R. Bhagat, D. Haddleton and C. Wan, *Materials*, 2016, **9**, 35.

40 J. Park, J. Joo, S. G. Kwon, Y. Jang and T. Hyeon, *Angew. Chem., Int. Ed.*, 2007, **46**, 4630–4660.

41 X. Peng, J. Wickham and A. Alivisatos, *J. Am. Chem. Soc.*, 1998, **120**, 5343–5344.

42 L. Zhang, Z. Su, F. Jiang, L. Yang, J. Qian, Y. Zhou, W. Li and M. Hong, *Nanoscale*, 2014, **6**, 6590–6602.

43 J. Wei, Y. Hu, Y. Liang, B. Kong, Z. Zheng, J. Zhang, S. P. Jiang, Y. Zhao and H. Wang, *J. Mater. Chem. A*, 2017, **5**, 10182–10189.

44 Z. Li, X. Huang, C. Sun, X. Chen, J. Hu, A. Stein and B. Tang, *J. Mater. Sci.*, 2017, **52**, 3979–3991.

45 S. Chu and A. Majumdar, *Nature*, 2012, **488**, 294.

46 X. Xu, C. Qi, Z. Hao, H. Wang, J. Jiu, J. Liu, H. Yan and K. Suganuma, *Nano-Micro Lett.*, 2018, **10**, 1.

47 Y. Han, P. Qi, S. Li, X. Feng, J. Zhou, H. Li, S. Su, X. Li and B. Wang, *Chem. Commun.*, 2014, **50**, 8057–8060.

48 W. Xia, A. Mahmood, R. Zou and Q. Xu, *Energy Environ. Sci.*, 2015, **8**, 1837–1866.

